PAPER

Extracting attosecond delays from spectrally overlapping interferograms

View the article online for updates and enhancements.

Extracting attosecond delays from spectrally overlapping interferograms

Inga Jordan and Hans Jakob Wörner

Laboratorium für Physikalische Chemie, ETH Zürich, Vladimir-Prelog-Weg 2, 8093 Zürich, Switzerland

E-mail: hwoerner@ethz.ch

CrossMark

Abstract

Attosecond interferometry is becoming an increasingly popular technique for measuring the dynamics of photoionization in real time. Whereas early measurements focused on atomic systems with very simple photoelectron spectra, the technique is now being applied to more complex systems including isolated molecules and solids. The increase in complexity translates into an augmented spectral congestion, unavoidably resulting in spectral overlap in attosecond interferograms. Here, we discuss currently used methods for phase retrieval and introduce two new approaches for determining attosecond photoemission delays from spectrally overlapping photoelectron spectra. We show that the previously used technique, consisting in the spectral integration of the areas of interest, does in general not provide reliable results. Our methods resolve this problem, thereby opening the technique of attosecond interferometry to complex systems and fully exploiting its specific advantages in terms of spectral resolution compared to attosecond streaking.

(Some figures may appear in colour only in the online journal)

1. Introduction

Attosecond interferometry was originally introduced as a technique for the temporal characterization of attosecond pulse trains [1]. In this context, it was called RABBIT (standing for *Reconstruction of attosecond beating by interference of two-photon transitions*) [2]. It is based on quantum-path interference using extreme-ultraviolet (XUV) radiation consisting of consecutive odd harmonic orders and an assisting infrared (IR) laser field at the fundamental frequency used to generate the XUV radiation. Ionization of the sample by the XUV pulses creates the *principle* photoelectron peaks, whereas the additional action of the IR field creates *sidebands* that are energetically located between the principal peaks. Under these conditions the intensities of the sidebands undergo oscillations as a function of the delay between the two fields, which was first observed by Paul *et al* [3]. This intensity modulation of each sideband can be expressed in terms of a cosine function with an overall phase offset ϕ:

$$A_{\text{SB}} \propto \cos(2\omega_0\tau \underbrace{-\Delta\phi_{\text{XUV}} - \Delta\phi_{\text{sys}}}_{\phi}). \quad (1)$$

Here, ω_0 is the IR-laser angular frequency, τ is the delay between XUV and fundamental laser pulses. $\Delta\phi_{\text{XUV}}$ corresponds to the difference in spectral phases of the involved harmonic orders and is related to the relative harmonic emission times. $\Delta\phi_{\text{sys}}$ is given by the difference of the phases of the two-photon matrix elements of the two quantum paths leading to the sideband SB. This quantity depends on the system and the final state in which it is left after ionization. Thus, $\Delta\phi_{\text{XUV}}$ enables the reconstruction of attosecond pulse trains, whereas $\Delta\phi_{\text{sys}}$ gives access to photoionization dynamics. It can approximately be further decomposed into the complex amplitudes of one-photon ionization and IR-driven continuum–continuum (cc) transitions [4, 5]. This decomposition takes the form of a simple sum of the individual phases of the XUV and cc transitions, when photoionization can be described by a single angular-momentum channel [6]. This separation is, however, only exact in the case of an initial atomic s state and breaks down in all other cases. The energy derivative of the phase of the one-photon matrix element is known as the Wigner delay, following the pioneering work of Wigner, Smith and Eisenbud [7, 8].
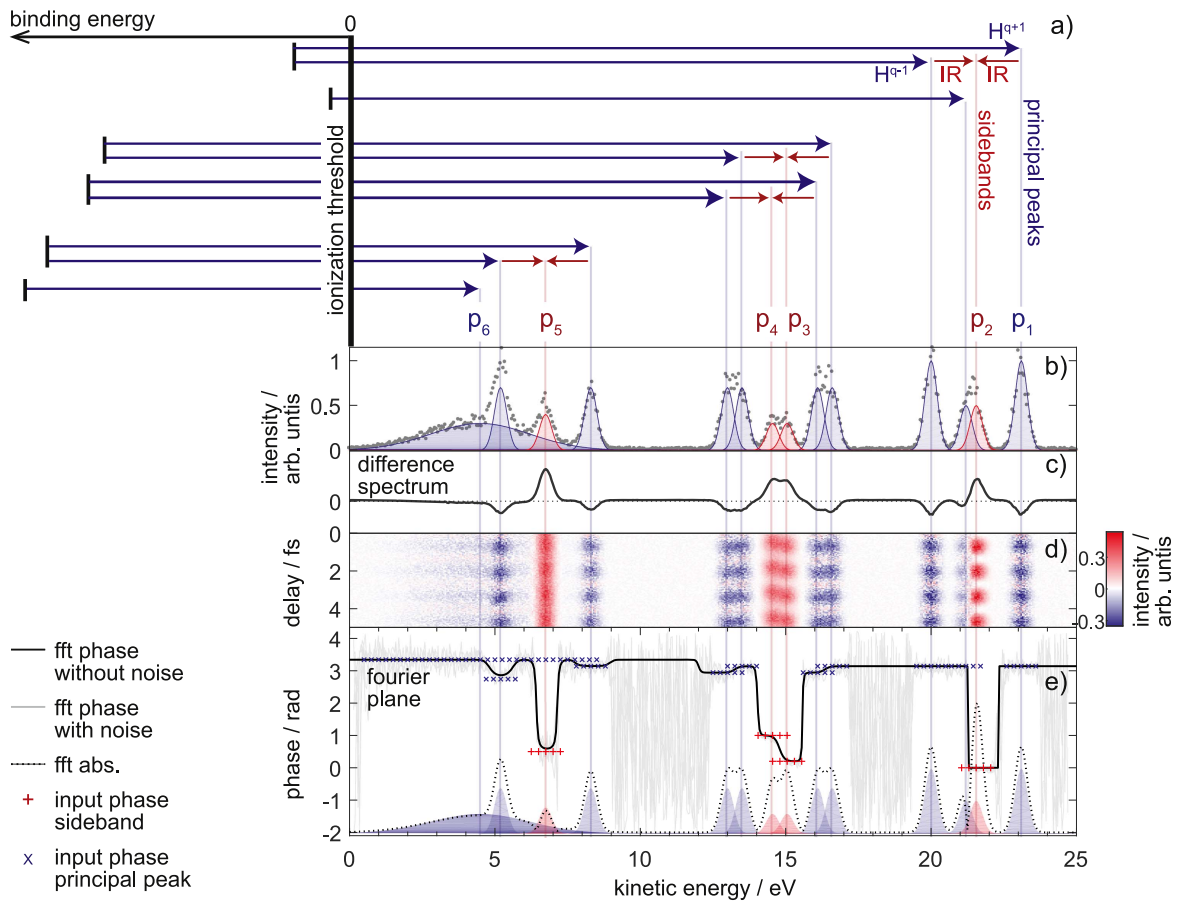
Figure 1. (a) Illustration of attosecond interferometry of a hypothetical system with six accessible electronic shells that is exposed to a pair of neighboring odd high-order harmonics and an assisting infrared laser field. Some quantum paths have been omitted for clarity. (b) Simulated photoelectron spectrum containing principal peaks (shown in blue) and side-band peaks (red). (c) Difference between an XUV+IR spectrum and an XUV-only spectrum. (d) Difference spectra as a function of the XUV-IR delay. (e) Amplitude (dotted line) and phase (full line) of the line-wise Fourier transform of the difference spectrogram, evaluated at the $2\omega_0$ oscillation component. The phases used as input for the principal and side-band oscillations are shown as blue and red crosses, respectively.

The first measurement of photoionization delays has actually been realized in the condensed phase using attosecond streaking [9], followed by the first application to neon atoms in the gas phase [10]. Attosecond interferometry has been first applied to measure the photoionization dynamics of argon [4, 11] and other atoms [12–16]. Recently, attosecond interferometry has been extended to molecules with the first measurement of attosecond delays in N_2O and H_2O [17] and to solids [18, 19]. These experiments have triggered considerable theoretical work on the photoionization dynamics of atoms [5, 6, 20–24], molecules [17, 25–28] and solids [29–33]. Both experimental and theoretical work has been reviewed in [34].

The photoelectron spectrum of most systems consists of more than one band, which leads to overlap between the photoelectron spectra created by multiple neighboring harmonic orders, overlap of sidebands and/or overlap between side-band and principal peaks. All of these situations are schematically illustrated in figures 1(a) and (b), which shows the hypothetical case of a system with 6 electronic shells that are being ionized by two neighboring harmonic orders, i.e. the simplest laser-field configuration required for attosecond interferometry. Some quantum paths have been omitted for clarity. The approach that has been followed in all published literature to date, except [16],

consisted in carefully choosing the spectral area of interest, with the goal of isolating the phase information contained in a particular sideband (see, e.g. [17–19, 35]). We will refer to this method as the 'spectral-integration' method. An alternative approach, introduced in [36], consists in analyzing the phase of the side-band oscillation as a function of the electron kinetic energy. This approach provides energy-resolved information but it does not resolve the problem of spectral overlap, which is the main topic of this article. We present an energy-resolved approach that goes beyond the method discussed in [36] and accounts for phase variation caused by spectral overlap.

In this article, we investigate the analysis of spectrally overlapping attosecond interferograms. We show that the spectral-integration method only provides reliable results when the spectral overlap is sufficiently small or the undesired spectral components do not modulate as a function of the XUV-IR delay. We propose two alternative methods, critically asses their performance and show that they do not suffer from the limitations of the spectral-integration method. The first method consists in performing a two-dimensional global fit of the attosecond interferogram in the kinetic-energy / time-delay domain. This method has been employed in our very recent determination of spin–orbit delays in the photoionization of xenon atoms [16],

where principal peaks and side-bands of the neighboring final state of the cation were spectrally overlapping. We present unpublished data from this work to illustrate the method in detail. The second method consists in Fourier transforming the attosecond interferogram along the time-delay axis and subsequently retrieving the phases of interest from an analysis of the complex-valued Fourier transform. This method is the most powerful one because it does not only correctly retrieve phases, even in the presence of extensive spectral overlap, but it does also account for a possible finite contrast in the attosecond interferograms, which is of relevance for future work on the role of decoherence on attosecond time scales.

2. Phase extraction

This section illustrates the three methods for extracting phase information from attosecond interferograms. We point out the advantages and disadvantages of each method in terms of accuracy and reproducibility by applying them to the same simulated attosecond interferogram (figure 1), which includes different types of spectral overlap between Gaussian-shaped peaks.

Principal and side-band peaks generated by the XUV- and IR-induced transitions illustrated in figure 1 a were assigned an individual amplitude (panel (b), maximum peak amplitude = 1) and a cosine-type oscillation with an individual modulation depth and phase (crosses and plus signs in panel (e)). Noise was simulated in both dimensions by a 25% random amplitude fluctuation and an offset by a random number between 0 and 0.025 for each point. The delay-averaged difference spectrum ((XUV+IR)-(XUV only)) is shown in panel (c). The representation of this difference spectrum as a function of the XUV-IR time delay yields the simulated attosecond interferogram shown in panel (d). Results of line-wise Fourier transform along the time-delay axis are shown for the $2\omega_0$ component in terms of amplitude and phase in panel (e). The solid black line corresponds to the phase extracted by line-wise Fourier transformation from a simulated spectrogram without noise. The light gray line represents phases associated with random amplitude fluctuations in the range of $\pm 25\%$ for each delay step. Apparently, the amplitude fluctuations of the spectrogram manifest themselves as a distribution of phases around the noise-free phase. The width of the phase distribution scales with the signal-to-noise ratio and the modulation depth. This behavior reflects the uncertainty expected from experimental data and demonstrates that several independent scans are usually necessary to retrieve correct phases, particularly for low-contrast oscillations.

The crosses and plus signs in figure 1(e) indicate the simulation input phases for the cosine functions. In the case of overlap-free spectral regions these phases are reproduced well

by the black and the gray line. This means that the input phases would be correctly retrieved by the spectral-integration method, as expected. However, regions of spectral overlap are found to oscillate with phases that result from the superposition of at least two oscillations. In these cases, the phases obtained from line-wise Fourier transformation do not reflect the simulation input phases but a certain value lying between them. Peaks p_3 and p_4 clearly demonstrate the phase variation along the kinetic-energy axis in the region of overlap between both peaks. In the case of p_5 and p_6 the overlap prevents extracting the input phase of p_5 using the integration method.

The absolute values of the FFT spectrogram are integrated along the frequency axis within the boundaries of the $2\omega_0$ oscillation (not shown) and compared to the input peaks in figure 1(e). The Fourier amplitude correlates with the oscillation amplitude and, assuming constant modulation depth over the peak width, reflects the peak shapes.

2.1. Spectral integration

The method used in most previous studies is the spectral-integration method, which is based on the identification of the spectral regions of interest, its integration along the kinetic-energy axis, followed by the retrieval via Fourier transformation or sine fitting of the obtained amplitude oscillation along the time-delay axis. Spectral integration is preferred over choosing a single cut for signal-to-noise reasons. Nevertheless, the same arguments pro or contra the integration method also apply to the analysis of slices through the spectrogram at individual kinetic energies.

The phase evolution over the kinetic-energy range of a photoelectron peak is of fundamental importance. Flatness is a prerequisite for the spectral-integration method to yield correct oscillation phases. Phase variation over the photoelectron peak is an indication for spectral overlap and the spectral-integration method would yield falsified phases. This becomes very clear in the simulated spectrogram in figure 1 for peaks p_3 and p_4, where the spectral region for integration would be very narrow and only at the opposite edges of both overlapping peaks. For peak p_5, however, the underlying principal-peak oscillation prevents the correct retrieval of the input phase based on the spectral-integration method.

It should be noted that a phase variation as a function of the kinetic energy can also have a physical origin, as demonstrated in [36]. However, the influence of possible spectral overlap has to be carefully examined beforehand.

Based on the discussion above, it becomes very clear that the phases in the regions of spectral overlap do not resemble the input phases of the involved oscillations. The deviation scales with the amount of overlap with the unwanted oscillation. Rephrased in mathematical terms, the sum of two sine functions

$$a_1 \sin(x + \phi_1) + a_2 \sin(x + \phi_2) = A \sin\left(x + \operatorname{atan2}\left[\begin{pmatrix} a_1 \\ a_2 \end{pmatrix} \cdot \begin{pmatrix} \sin(\phi_1) \\ \sin(\phi_2) \end{pmatrix}, \begin{pmatrix} a_1 \\ a_2 \end{pmatrix} \cdot \begin{pmatrix} \cos(\phi_1) \\ \cos(\phi_2) \end{pmatrix}\right]\right)$$
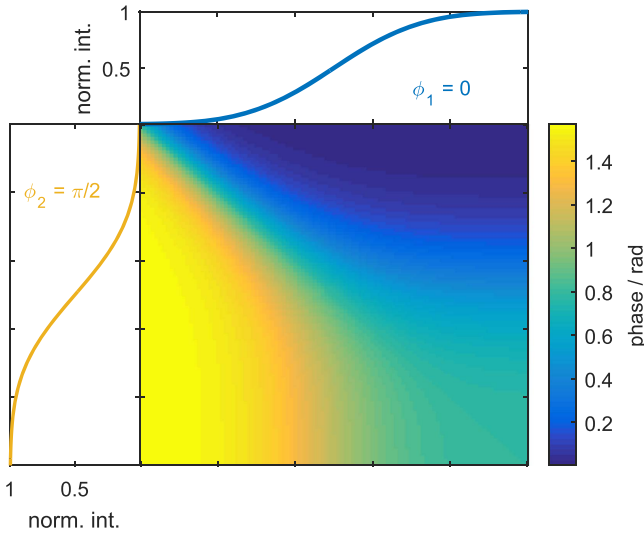
(2)

Figure 2. Center panel: effective phase of the sum of two superimposed oscillations as a function of the individual oscillation amplitudes. Amplitude a_1 of component 1, which is assigned an oscillation phase of $\phi_1 = 0$ rad is shown in the upper panel, amplitude a_2 of component 2 assigned $\phi_2 = \pi/2$ is shown in the left panel.

has a total phase that is the weighted average of the underlying oscillations. The phase of the superimposed oscillation as a function of the amplitudes a_1 and a_2 of the underlying oscillations was computed using equation (2) and is shown in figure 2. The two phases, $\phi_1 = 0$ and $\phi_2 = \pi$, were assigned to the two involved contributions. The phase of one component transits gradually to the phase of the other component according to their relative amplitudes.

These results show that spectral integration must only be performed in overlap-free regions. However, spectral overlap with a non-modulating band, i.e. a constant amplitude offset, will not influence the extracted phase. Therefore, the restriction only applies to spectral overlap where the unwanted contributions are associated with non-negligible modulation depths.

2.2. Two-dimensional fit

The global fitting is based on a two-dimensional representation of the attosecond interferogram. Photoelectron spectra generated with only XUV radiation are fitted on the kinetic-energy axis using Gaussian functions. The fitted peak positions are fed into the fit of the XUV+IR spectrum where sideband peaks are added. Optionally, the delay-integrated difference spectrum can also be fitted using the results from the fit of the XUV+IR-spectrum. This bears the advantage, that peak positions can be located more precisely in the difference spectrum, since sidebands and principal peaks appear with opposite signs. After the delay-integrated peak information was extracted, each photoelectron peak is assigned a cosine oscillation with a constant phase over the entire peak width. Amplitudes, modulation depths and phases of the oscillations are fitted for each peak individually, the frequency being the global fit parameter for all oscillations.

Two-dimensional fitting of an XUV+IR spectrogram derived from the difference spectrogram shown in figure 1 is presented together with the residuals in figure 3. The spectrogram was separated into four slices and each slice was treated separately in order to maintain a reasonable amount of fit parameters per slice. Otherwise, the global minimum is less likely to be found, and, in the case of strongly varying peak amplitudes, a weighting function would be necessary. The slices have to be chosen such that they contain the sets of sideband oscillations whose relative phases will be compared. The simulated spectrogram is well reproduced by the fit and no systematic deviations can be observed in the residuals.

For the least-squares fitting to be reproducible, a dependence on the initial guesses has to be excluded. Such a dependence could be observed in the presence of a high density of local minima, particularly if the spectral features do not support the number of fit parameters required by the model.

In order to estimate the reproducibility of the fit parameters for the simulated spectrogram presented in figure 3, initial guesses have been varied randomly within defined boundaries for each parameter. The resulting phases from 100 fit runs are shown in figure 4 for the isolated peak p_1 and in figure 5 the overlap situation between p_5 and p_6.

In the case of the overlap-free oscillation (referring to figure 4) associated with the peak p_1 in figure 1(e), the fit converges mostly to the input value within a defined distribution (figure 4(b)). Residuals are referenced to the lowest value for a given noise-level setting. The width of the phase spread was found to depend only on the noise level and the modulation depth (not shown here). Fit failure in the case of poorly guessed initial values manifests itself in significantly higher residuals (figure 4(a)) such that fit failure and residuals are clearly correlated. In the absence of noise, the input phase is reproduced with negligible deviations by the fit (figure 4(c)). For one given noise configuration, variation of initial guesses has only a minor effect on the retrieved phase (figure 4(d)). The phases in figure 4(d) are shown with respect to the mean of the obtained distribution.

In the case of oscillations affected by peak overlap (referring to peak p_5 in figure 5) the fit performs, in general, comparably well as for the overlap-free oscillation discussed above. Low residuals can be taken as a criterion for a successful fit. In contrast to the integration method, the phase of the oscillation of peak p_5 is retrieved correctly by the fit for both, noise-free and noisy, spectrograms (compare figures 5(b) and (c)). However, repeatedly fitting the spectral slice containing p_5 and varying only the initial guesses shows that the quality of those guesses starts to play a role (compare figure 5(d)). Nevertheless, sufficient sampling of the initial-guess space still ensures that the correct phases are extracted.

Besides estimating the repeatability of the two-dimensional fit for different initial guesses, the accuracy was quantified as well. This was studied by moving the two peaks on top of each other in a stepwise manner and simulating and fitting a spectrogram at each step. This distance scan was repeated 100 times. Amplitude fluctuations of 25% and 100% were generated at each scan step for each distance scan
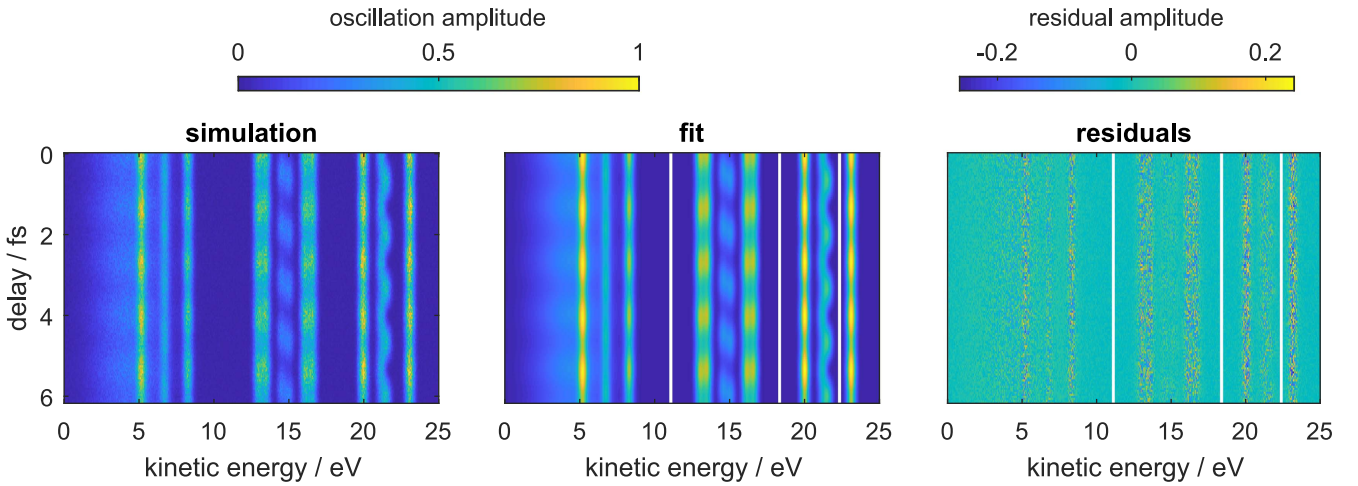
Figure 3. Two-dimensional global fit of a simulated attosecond interferogram. The spectrogram on the left corresponds to the simulation in figure 1, however, instead of the difference spectrogram the XUV+IR spectrogram as a function of the XUV-IR delay is shown. The simulation was fitted in both dimensions simultaneously with a global frequency for all oscillation contributions (central panel). Vertical white lines represent the borders between the spectral slices that were treated separately. The residuals (absolute square of the difference between fit and simulation) is shown on the right.
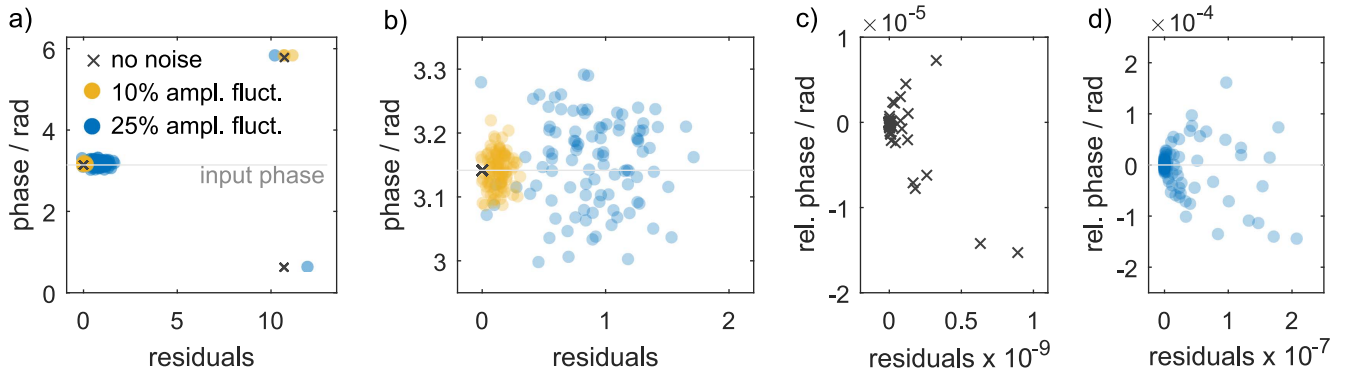

Figure 4. Reproducibility of fitted phases using the two-dimensional fitting approach at three different noise levels (noise-free, 10% and 25% amplitude fluctuations) for peak 1 (referring to figure 1). Residuals refer to the sum of squared differences between simulation and fit. (a) full distribution of fitted phases from 100 fit runs, with newly generated noise and guess values for each fit run. (b) Zoom into (a) at low residuals. (c) Retrieved phases relative to the input phase (π) for repeated fitting (100 runs) of the noise-free spectrogram, with newly generated guess values for each fit run (zoomed at lowest residuals). (d) Phases from repeated fitting of a single spectrogram (25% noise level, not changing between fit runs, 100 fit runs), with newly generated guess values for each fit run. Phases are shown relative to the mean of the obtained distribution.

individually. Similarly, initial guesses were varied for each single fit. The extracted phases are shown in the lower panel of figure 6 and the configuration of the peaks is indicated in the upper panel. The peak distance is given in % of the peak full-width-at-half-maximum (FWHM). Error bars refer to the standard deviation associated with 100 fit runs per step. All fit results were considered (no discrimination based on residuals).

The retrieved phases depend on the initial guesses if the peaks are closer than 50% of their FWHM and deviate significantly from the correct values, indicated by the gray dotted lines in figure 6. The error bars scale with the noise level. It is also found that the critical distance depends on the total points per peak, i.e. peaks can approach more closely in the case of large FWHM compared to narrow peaks on the same kinetic energy grid. In summary, the two-dimensional fit is capable of handling spectral overlap, however both accuracy and

precision depend on the extent of overlap and the retrieved phases might depend on the initial guesses.

This approach was applied to attosecond interferograms, obtained by ionizing the 5p shell of xenon, which gives rise to two photoelectron peaks, associated with the $^2P_{1/2}$ and $^2P_{3/2}$ levels of the electronic ground state of Xe^+. Since these two levels are separated by 1.31 eV, which is close to the energy of one 800 nm photon (1.55 eV), this case is a nice illustration of overlap between the principal photoelectron peak and the neighboring side-band peak associated with the other final state of the cation (cp. figure 1(a), upper kinetic energy region). Figure 7 shows the experimental photoelectron spectra generated from XUV-only (blue) and XUV+IR (red) radiation in panel (a), followed by the difference spectrum in panel (b) and its variation with the XUV-IR delay in panel (c). In our experimental work, we found that the signal-to-noise ratio of the attosecond interferogram can be considerably
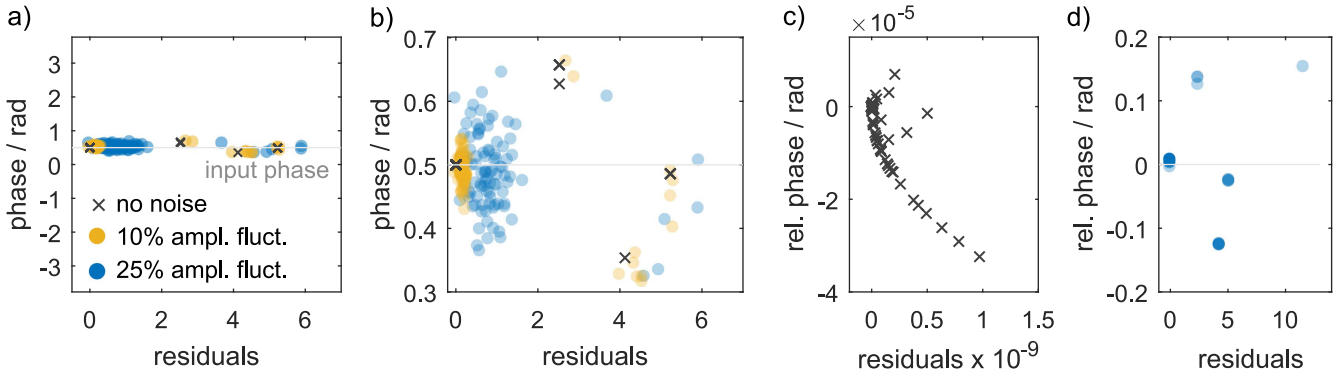
Figure 5. Reproducibility of fitted phases using the two-dimensional fitting approach at three different noise levels (noise-free, 10% and 25% amplitude fluctuations) for peak 5 (referring to figure 1). Residuals refer to the sum of squared differences between simulation and fit. (a) Full distribution of fitted phases from 100 fit runs, with newly generated noise and guess values for each fit run. (b) Zoom into (a) at low residuals. (c) Retrieved phases relative to the input phase (π) for repeated fitting (100 runs) of the noise-free spectrogram, with newly generated guess values for each fit run (zoomed at lowest residuals). (d) Phases from repeated fitting of a single spectrogram (25% noise level, not changing between fit runs, 100 fit runs), with newly generated guess values for each fit run. Phases are shown relative to the mean of the obtained distribution.
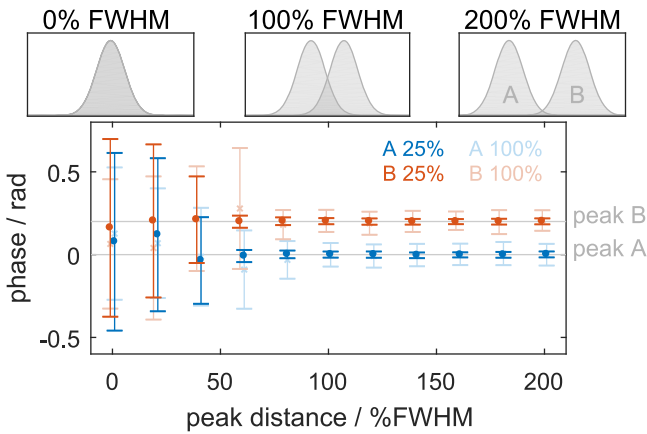

Figure 6. Accuracy of the two-dimensional fit as a function of the peak distance expressed in % of the peak FWHM for two different noise levels (25% and 100%). Top panel: peaks used to simulate the spectrogram at 3 different distances (0% corresponds to complete overlap). Bottom panel: phases extracted by the two-dimensional fit as a function of the peak separation. Error bars refer to standard deviation from 100 fit runs. Gray lines indicate input values.

Figure 7. Experimental data from attosecond interferometry of spin–orbit delays in the photoionization of Xe. (a) Photoelectron spectra (blue: XUV only, red: XUV+IR), (b) difference spectrum, (c) difference spectrum as a function of the XUV-IR delay, (d) two-dimensional global fit of the data in panel (c).

improved by recording photoelectron spectra as the difference between XUV+IR and XUV-only photoelectron spectra on a single-shot basis. The great advantage of this approach, used in [16, 17], is that the effect of XUV-intensity and target-density fluctuations are minimized. The partial overlap of each principal peak with the side-band of the neighboring harmonic leads to the characteristic observed dispersion-type line shapes. Positively signed peaks are associated with spectral regions dominated by sideband contributions (shown in red) whereas negatively signed peaks are associated with spectral regions dominated by principal peaks (shown in blue).

The spectrogram shown in figure 7(c) was divided into 3 kinetic-energy regions such that each region contained the same sideband orders for the two spin–orbit components. Cutting the spectrogram into such regions reduces the number of fitting parameters per spectrum and avoids a strong
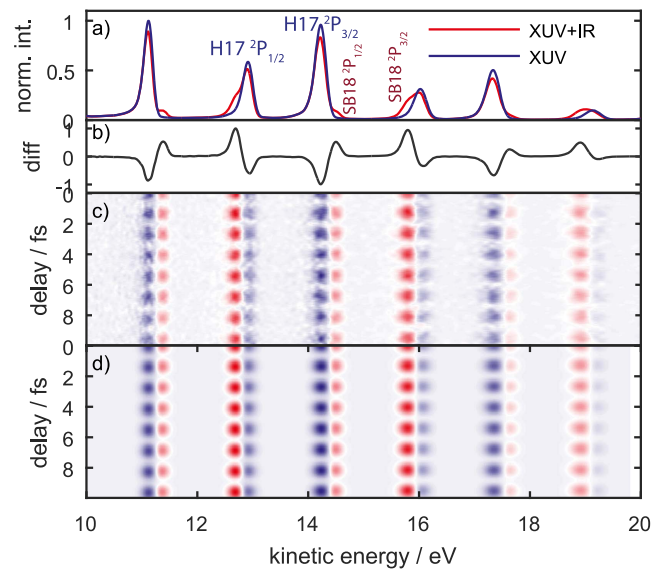
variation of the amplitudes across the spectrum. Otherwise spectral regions of high intensity would be fitted more precisely than those of low intensity. Panel (d) shows the results of the two-dimensional fits of the experimental spectrogram in panel (c). The comparison of the two panels nicely illustrates the very high fidelity of this approach. The delays extracted from these measurements are $\tau_{3/2} - \tau_{1/2} = 11 \pm 4$ as, 31 ± 5 as, 33 ± 6 as, for the side-band orders 16, 18 and 20, respectively [16].

2.3. Complex fit

The complex fit starts with the same fitting of XUV-only and XUV+IR spectra as the two-dimensional fit approach, but

instead of fitting the actual intensity modulations in a two-dimensional spectrogram, the attosecond interferogram is Fourier transformed line-by-line along the time-delay axis and integrated within the boundaries of the $2\omega_0$ oscillation peak to yield a one-dimensional complex-valued array along the kinetic-energy axis. Peak shapes and oscillation amplitudes are now encoded in the absolute value of the Fourier transform whereas the phase variation as a function of the kinetic energy reflects the transition between input phases, weighted by the amount of overlap. We note that the first step of our approach is similar to the concept of the rainbow-RABBIT [36], which consists in interpreting the phase of the Fourier transform as a function of the kinetic energy. This approach alone does however not resolve the problem of spectral overlap, which is demonstrated by the fact that the thick line in figure 1(e) does not coincide with the input phases, e.g. in the case of p_5, given by the red crosses. Our complex-fit method therefore goes one step further and consists in a direct fit of the complex-valued Fourier transform such that the actual phase transition is properly reproduced. While in [36] any energy-dependent phase variation is assigned to a physical origin, i.e. a resonance, our results show that such a phase variation can also result from spectral overlap.

Assigning a complex-valued fit parameter $z_j = a_j + ib_j$ to each band, $p_j(E)$, obtained from fitting delay-integrated XUV+IR spectra and subsequent summation gives an one-dimensional complex array, $I(E)$, which can be fitted to the Fourier-transform.

$$I(E) = \sum_j p_j(E)\mathrm{e}^{z_j} = \sum_j \underbrace{\mathrm{e}^{a_j} p_j(E)}_{A_j(E)}\mathrm{e}^{ib_j}. \qquad (3)$$

Each oscillation component j is now interpreted in terms of its Fourier amplitude A_j related to the oscillation amplitude, and the phase b_j, being the imaginary part of the complex fit parameter z_j. In the present work, we use Gaussian functions for $p_j(E)$, but our method is not restricted to this particular choice. In general, the deconvolution described in equation (3) reduces the number of fit parameters compared to the full two-dimensional fit on the one hand and the total array size entering the fitting procedure on the other hand. The fit is thus much more likely to rapidly converge to the global minimum.

The complex fit was applied to the simulated spectrogram in figure 1 and the results are presented in figure 8. Retrieved phases and amplitudes are shown in the upper panel, real and imaginary parts of the fit array in the lower panel. Circles indicate phases and amplitudes (upper panel of figure 8) or real and imaginary parts (lower panel) obtained from the line-wise Fourier transformation of the noise-free simulated spectrogram and integration within the $2\omega_0$ peak width along the frequency axis (compare lower panel in figure 1). The fit reproduces the input spectrogram with very high fidelity. The dependence on the initial guesses and peak separation was studied here as well and is shown in figures 9 and 10, respectively. Since no absolute phases can be inferred from the Fourier transform, the fit results have to be presented to a reference. In the case of the simulated spectrogram from
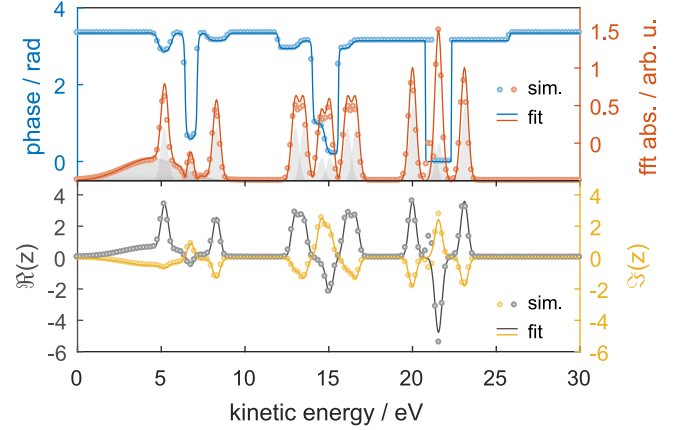

Figure 8. Results of a complex-valued fit to the Fourier transform of the difference spectrogram from figure 1(e). Solid lines represent phases and angles (upper panel), and real and imaginary parts (lower panel) of the fit, circles represent the outcome of the line-wise Fourier-transform of a noise-free simulated difference spectrogram.

figure 1, phases are referenced to the overlap-free oscillation of p_1. When studying the peak separation, the phases of both peaks are referenced against each other.

The precision of the complex fit is very good. This is visualized in figures 9(a) and (b), where the oscillation phase of peak p_5 is shown. Particularly for very low residuals, the retrieved phases are almost identical. Compared to the two-dimensional fit, the distribution of phases at low residuals is very narrow. We found that the input phase is not exactly reproduced for this particular pulse overlap, however, the deviation is less than 1% and hence much better, than the spectral-integration method. This deviation is attributed to the underlying oscillation of p_6, since the phase of the background-free oscillation at 20 eV is reproduced with high accuracy and precision (see figure 9(c)). Varying the initial guesses 100 times for the same spectrogram with a 25% noise level does reveal a dependency on the fit parameter (see figure 9(d)), but also the correct phases are found when discarding fit runs associated with too high residuals.

Figure 10 illustrates the accuracy of the complex fit, using the same example as in figure 6, i.e. that of two Gaussian peaks with a variable separation. The direct comparison of the two figures shows the clear superiority of the complex-fit approach, which yields nearly perfect results for all separations. The error bars are also smaller in general, with the exception of the case of full overlap. The performance of the complex fit, however, depends on the delay range. In the study presented here, the delay was set to 10 fs with a 0.2 fs step size. If the delay range becomes shorter, the energy-dependent phase exhibits more noise and fitting becomes less accurate.

The modulation depths are readily extracted from the complex fit through the real part of the fitted complex number z. As equation (3) implies, the Fourier amplitude and therefore the oscillation amplitude of a sideband peak is given by the product of the spectral intensity $p_j(E)$ and $\mathrm{e}^{\Re(z_j)}$. Hence,
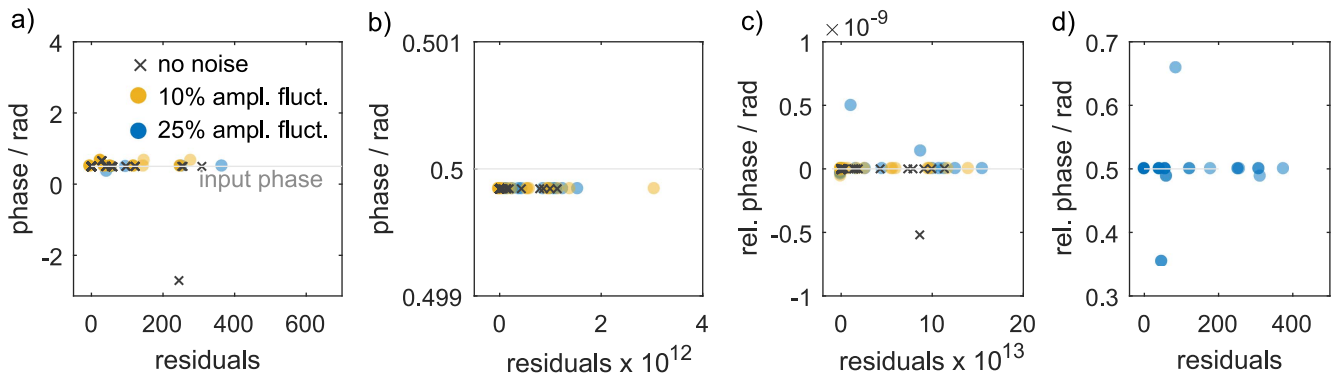
Figure 9. Reproducibility of fitted phases using the complex-valued fitting approach at three different noise levels (noise-free, 10% and 25% amplitude fluctuations). Residuals refer to the sum of squared differences between simulation and fit. (a) Full distribution of fitted phases from 100 fit runs for peak p_5, with newly generated noise and guess values for each fit run. (b) Zoom into (a) at low residuals. (c) Relative phase between p_1 and the background-free oscillation at 20 eV, with newly generated guess values for each fit run (zoomed at lowest residuals). (d) Phases for p_5 from repeated fitting of a single spectrogram (25% noise level, not changing between fit runs, 100 fit runs), with newly generated guess values for each fit run. Phases are shown relative to the mean of the obtained distribution.
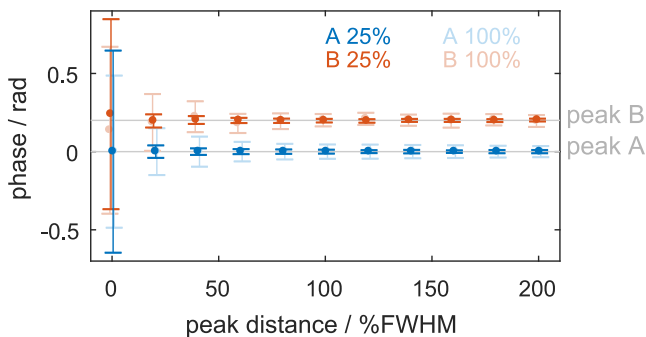

Figure 10. Accuracy of the complex-valued fit as a function of peak separation. Error bars refer to standard deviation from 100 fit runs. Gray lines indicate input values.

the term $e^{\Re(z_j)}$ reflects the oscillating fraction of the sideband intensity ($p_j(E)$ is the delay-integrated peak intensity). Its numerical value is expected to be 1 in case the sideband amplitude modulates between the baseline and its maximum value. The modulation depth is defined as the ratio between the oscillation amplitude and the oscillation offset (delay-integrated sideband intensity). Thus, the modulation depth is directly obtained from $p_j(E) * e^{\Re(z_j)} / p_j(E) = e^{\Re(z_j)}$.

3. Conclusion and outlook

We have systematically analyzed the performance of three different approaches to retrieve photoionization delays from attosecond interferograms. We have found that the widely used technique of spectral integration is problematic in the presence of spectral overlap when the undesired spectral component possesses a non-negligible modulation contrast. We have introduced two alternative techniques that overcome these limitations. The first consists in a global two-dimensional fit of the relevant parts of the attosecond interferogram. This technique has been successfully applied to extract spin–orbit delays in the electronic ground state of Xe$^+$ [16] and has been illustrated in more detail here. The second technique

consists in Fourier-transforming the attosecond interferogram along the time-delay axis, followed by a multi-component fit of the complex Fourier-transform using the principal components determined in the analysis of XUV-only and XUV+IR spectra. Both techniques are applicable to the analysis of spectrally overlapping attosecond interferograms and will be of great use in the analysis of photoionization delays of molecules [17], solids [18, 19] and liquids [37].

Acknowledgments

ORCID iDs

Hans Jakob Wörner ⓘ https://orcid.org/0000-0002-8877-0872

References

[1] Véniard V, Taïeb R and Maquet A 1996 *Phys. Rev. A* **54** 721
[2] Muller H 2002 *Appl. Phys. B* **74** s17
[3] Paul P M *et al* 2001 *Science* **292** 1689
[4] Klünder K *et al* 2011 *Phys. Rev. Lett.* **106** 143002
[5] Dahlström J M, L'Huillier A and Maquet A 2012 *J. Phys. B: At. Mol. Opt. Phys.* **45** 183001
[6] Dahlström J *et al* 2013 *Chem. Phys.* **414** 53
[7] Wigner E P 1955 *Phys. Rev. A* **98** 145
[8] Smith F T 1960 *Phys. Rev.* **118** 349
[9] Cavalieri A L *et al* 2007 *Nature* **449** 1029
[10] Schultze M *et al* 2010 *Science* **328** 1658
[11] Guénot D *et al* 2012 *Phys. Rev. A* **85** 053424
[12] Palatchi C *et al* 2014 *J. Phys. B: At. Mol. Opt. Phys.* **47** 245003
[13] Guénot D *et al* 2014 *J. Phys. B: At. Mol. Opt. Phys.* **47** 245602
[14] Baggash M and Rottke H 2015 *Phys. Rev. A* **92** 013424

[15] Heuser S *et al* 2016 *Phys. Rev.* A **94** 063409
[16] Jordan I *et al* 2017 *Phys Rev* A **95**
[17] Huppert M, Jordan I, Baykusheva D, von Conta A and Wörner H J 2016 *Phys. Rev. Lett.* **117**
[18] Locher R *et al* 2015 *Optica* **2** 405
[19] Tao Z *et al* 2016 *Science* **353** 62
[20] Kheifets A S and Ivanov I A 2010 *Phys. Rev. Lett.* **105** 233002
[21] Nagele S *et al* 2011 *J. Phys. B: At. Mol. Opt. Phys.* **44** 081001
[22] Pazourek R, Feist J, Nagele S and Burgdörfer J 2012 *Phys. Rev. Lett.* **108** 163001
[23] Kheifets A S 2013 *Phys. Rev.* A **87** 063404
[24] Maquet A, Caillat J and Taïeb R 2014 *J. Phys. B: At. Mol. Opt. Phys.* **47** 204004
[25] Ivanov I A, Kheifets A S and Serov V V 2012 *Phys. Rev.* A **86** 063422
[26] Hockett P, Frumker E, Villeneuve D M and Corkum P B 2016 *J. Phys. B: At. Mol. Opt. Phys.* **49** 095602

[27] Baykusheva D and Wörner H J 2017 *J. Phys. B: At. Mol. Opt. Phys.* **50** 078002
[28] Baykusheva D and Wörner H J 2017 *J. Chem. Phys.* **146** 124306
[29] Zhang C-H and Thumm U 2009 *Phys. Rev. Lett.* **102** 123601
[30] Lemell C, Solleder B, Tőkési K and Burgdörfer J 2009 *Phys. Rev.* A **79** 062901
[31] Baggesen J C and Madsen L B 2009 *Phys. Rev.* A **80** 030901
[32] Borisov A G, Sánchez-Portal D, Kazansky A K and Echenique P M 2013 *Phys. Rev.* B **87** 121110
[33] Liao Q and Thumm U 2014 *Phys. Rev.* A **89** 033849
[34] Pazourek R, Nagele S and Burgdörfer J 2015 *Rev. Mod. Phys.* **87** 765
[35] Haessler S *et al* 2009 *Phys. Rev.* A **80** 011404
[36] Gruson V *et al* 2016 *Science* **354** 734
[37] Jordan I, Huppert M, Brown M A, van Bokhoven J A and Wörner H J 2015 *Rev. Sci. Instrum.* **86** 123905